

RAF inhibitors that evade paradoxical MAPK pathway activation

Chao Zhang¹, Wayne Spevak¹, Ying Zhang¹, Elizabeth A. Burton¹, Yan Ma¹, Gaston Habets¹, Jiazhong Zhang¹, Jack Lin¹, Todd Ewing¹, Bernice Matusow¹, Garson Tsang¹, Adhirai Marimuthu¹, Hanna Cho¹, Guoxian Wu¹, Weiru Wang¹, Daniel Fong¹, Hoa Nguyen¹, Songyuan Shi¹, Patrick Womack¹, Marika Nespi¹, Rafe Shellooe¹, Heidi Carias¹, Ben Powell¹, Emily Light¹, Laura Sanftner¹, Jason Walters¹, James Tsai¹, Brian L. West¹, Gary Visor¹, Hamid Rezaei¹, Paul S. Lin¹, Keith Nolop¹, Prabha N. Ibrahim¹, Peter Hirth¹ & Gideon Bollag¹

Oncogenic activation of BRAF fuels cancer growth by constitutively promoting RAS-independent mitogen-activated protein kinase (MAPK) pathway signalling¹. Accordingly, RAF inhibitors have brought substantially improved personalized treatment of metastatic melanoma^{2–5}. However, these targeted agents have also revealed an unexpected consequence: stimulated growth of certain cancers^{6–9}. Structurally diverse ATP-competitive RAF inhibitors can either inhibit or paradoxically activate the MAPK pathway, depending whether activation is by BRAF mutation or by an upstream event, such as RAS mutation or receptor tyrosine kinase activation^{10–12}. Here we have identified next-generation RAF inhibitors (dubbed ‘paradox breakers’) that suppress mutant BRAF cells without activating the MAPK pathway in cells bearing upstream activation. In cells that express the same HRAS mutation prevalent in squamous tumours from patients treated with RAF inhibitors, the first-generation RAF inhibitor vemurafenib stimulated *in vitro* and *in vivo* growth and induced expression of MAPK pathway response genes; by contrast the paradox breakers PLX7904 and PLX8394 had no effect. Paradox breakers also overcame several known mechanisms of resistance to first-generation RAF inhibitors. Dissociating MAPK pathway inhibition from paradoxical activation might yield both improved safety and more durable efficacy than first-generation RAF inhibitors, a concept currently undergoing human clinical evaluation with PLX8394.

Selective RAF inhibitors including vemurafenib¹³ and dabrafenib¹⁴ have demonstrated both objective tumour response and, in the case of vemurafenib, overall survival benefit in mutant BRAF^{V600}-driven melanoma. The clinical effectiveness of RAF inhibitors depends on near-complete abolition of the MAPK pathway output in tumours harbouring BRAF mutations¹³. However, these compounds paradoxically activate

the MAPK pathway in cells bearing oncogenic RAS or elevated upstream receptor signalling^{10–12}. This paradox can promote cellular proliferation and manifest clinically with progression of cutaneous squamous cell carcinomas (cuSCC) and keratoacanthomas, sometimes within weeks of therapy initiation^{6,15}. These paradox-induced skin tumours have an uncharacteristically high incidence of RAS mutations^{6,16}, raising the concern that the same mechanism might accelerate progression of other RAS-driven cancers. Recent case reports of increased incidence of primary melanomas⁷ and progression of RAS-mutant leukaemia and colon carcinoma during RAF inhibitor treatment^{8,9} add weight to the concern. Although combination with MEK inhibition represents one strategy to combat paradoxical activation, and such combinations did show improved clinical responses^{17,18}, the combination of these two costly agents yields increased adverse events, and resistance still develops. Our strategy to develop next-generation RAF inhibitors is thus to design potent BRAF^{V600} mutant inhibitors that avoid paradoxical activation of MAPK signalling.

Vemurafenib analogues with variable terminal sulfonamide and sulfamide substitutions were screened against a panel of cell lines for compound-induced change in phospho-ERK1/2 (T202/Y204, pERK). For each compound, the dissociation of pERK inhibition from activation (dubbed ‘ERK pathway inhibition index’ or EPII) was expressed as the ratio between the compound’s mean pERK activation half-maximum effective concentration (EC₅₀) in three RAS mutant cell lines (murine cuSCC cell line B9, human melanoma cell line IPC-298, and human colorectal carcinoma cell line HCT116, Table 1), and the compound’s mean pERK inhibition half-maximum inhibitory concentration (IC₅₀) in two BRAF^{V600E} melanoma cell lines (A375 and COLO829, Table 1). The EPIIs for vemurafenib and dabrafenib were

Table 1 | Comparison of the *in vitro* profile* of first-generation BRAF inhibitors with a paradox breaker

| Compound | Biochemical IC ₅₀ (μM) | | | pERK inhibition IC ₅₀ (μM) | | pERK activation EC ₅₀ (μM)† | | | EPII‡ |
|-------------|-----------------------------------|-----------------|-----------------|---------------------------------------|------------------|--|----------------|-----------------|---------|
| | BRAF ^{V600E} | BRAF | CRAF | A375 | COLO829 | B9 | IPC-298 | HCT116 | |
| Vemurafenib | 0.031 (±0.004) | 0.1 (±0.02) | 0.048 (±0.004) | 0.032 (±0.007) | 0.041 (±0.008) | 0.36 (±0.08) | 0.54 (±0.12) | 0.34 (±0.07) | 11 |
| PLX4720 | 0.013 (±0.005) | 0.16 (±0.03) | 0.007 (±0.003) | 0.044 (±0.006) | 0.039 (±0.023) | 0.24 (±0.03) | 0.4 (±0.05) | 0.29 (±0.17) | 7 |
| PLX7683 | 0.029 (±0.021) | 1.1 (±0.6) | 0.44 (±0.23) | 0.98 (±0.75) | 1.7 (±0.82) | >200 | >200 | >200 | >100 |
| PLX7904 | 0.0042 (±0.0006) | 0.14 (±0.02) | 0.091 (±0.014) | 0.016 (±0.005) | 0.018 (±0.005) | >200 | >200 | >200 | >10,000 |
| PLX8394 | 0.0038 (±0.0016) | 0.014 (±0.004) | 0.023 (±0.04) | 0.0035 (±0.0012) | 0.0021 (±0.0012) | >200 | >200 | >200 | >50,000 |
| PLX5568 | 0.58 (±0.07) | 0.19 (±0.02) | 0.021 (±0.002) | >10 | >10 | 5.1 (±2.5) | 3.2 (±1.9) | 7 (±3.2) | <0.5 |
| Sorafenib | 0.35 (±0.04) | 0.072 (±0.008) | 0.011 (±0.002) | 4.4 (±1.3) | 2 (±1.2) | 0.025 (±0.005) | 0.019 (±0.01) | 0.086 (±0.04) | 0.01 |
| Dabrafenib | 0.0054 (±0.0015) | 0.0027 (±0.001) | 0.0015 (±0.001) | 0.001 (±0.001) | 0.005 (±0.003) | 0.01§ (±0.005) | 0.01§ (±0.005) | 0.003§ (±0.002) | ~4 |
| PLX7922 | 0.012 (±0.008) | 1.1 (±0.4) | 0.053 (±0.006) | 0.01 (±0.003) | 0.014 (±0.008) | >10 | 3.3 (±2.4) | >10 | >500 |

*Mutational status of the cell lines: A375, BRAF^{V600E}, homozygous; COLO829, BRAF^{V600E}, heterozygous; B9, HRAS^{Q61L}; IPC-298, NRAS^{Q61L}; HCT116, KRAS^{G13D}. Each value is an average of more than four experiments. Values in parenthesis, s.e.m.

†EC₅₀, the concentration increasing pERK to 50% compared with the positive control, 10 μM PLX4720.

‡ERK pathway inhibition index (EPII), the ratio between mean pERK activation EC₅₀ and mean pERK inhibition IC₅₀.

§Using the rising portion of the concentration–response curve (Fig. 3c).

¹Plexikon Inc., 91 Bolivar Drive, Berkeley, California 94710, USA.

11 and 4, respectively. Among the compounds that exhibited more than 100-fold EPII was a molecule (PLX7683, Fig. 1a and Table 1) that contained an *N*-ethylmethyl-sulfamide moiety in lieu of the propyl-sulfonamide tail of vemurafenib. Optimization of this series of compounds by substitution on the 5-position of the 7-azaindole scaffold generated PLX7904 (Fig. 1a), which potently inhibited pERK in BRAF^{V600E} cells but showed essentially no pERK activation in RAS mutant cell lines at the concentrations tested (Table 1, Fig. 1b and Extended Data Fig. 1). PLX7904 was also evaluated in the human SCC cell line A431 and the human breast adenocarcinoma cell line SKBR3 as these cells achieve MAPK pathway activation by upstream signals feeding into RAS (through overexpression of epidermal growth factor receptor (EGFR) and human epidermal growth factor receptor 2 (HER2), respectively). Unlike vemurafenib, PLX7904 did not increase pERK levels in these cells (Fig. 1c). In biochemical assays using recombinant kinases, PLX7904 showed preferential inhibition of the mutated BRAF^{V600E} over wild-type

BRAF and CRAF and a level of kinase selectivity comparable to that of vemurafenib¹³ (Supplementary Table 1).

PLX7904 inhibited the *in vitro* growth of two aforementioned melanoma cell lines (A375 and COLO829) and an additional human colorectal cancer cell line COLO205 that expressed BRAF^{V600E} with IC₅₀ values of 0.17 μ M, 0.53 μ M, and 0.16 μ M, respectively, on a par with vemurafenib IC₅₀ values in the same assays (0.33 μ M, 0.69 μ M, and 0.25 μ M, respectively). Consistent with this *in vitro* result, PLX7904 and vemurafenib produced similar anti-tumour effects in a subcutaneous COLO205 xenograft model (Fig. 1e) with matching doses (25 mg per kg twice daily) and plasma exposures (steady-state area under the curve \approx 200,000 ng ml⁻¹ h).

Recent analyses^{6,16} of the cuSCC and keratoacanthoma lesions excised from vemurafenib recipients revealed that up to 60% of the specimens harboured RAS mutations, mostly HRAS^{Q61L}, supporting an important role of RAS mutation in BRAF inhibitor-induced cuSCC. The B9 cuSCC mouse cell line expresses the same activated HRAS^{Q61L} allele¹⁹. In soft agar, both vemurafenib and its analogue PLX4720 stimulated B9 colony formation at concentrations similar to the growth inhibitory IC₅₀ values in A375, COLO829, and COLO205 cells, whereas PLX7904 did not (Fig. 1d). When tested *in vivo*, subcutaneous B9-tumour growth was accelerated by vemurafenib but not by the equally potent BRAF^{V600E} inhibitor PLX7904 when administered at the same dose (Fig. 1f).

We compared the gene expression changes in B9 cells treated overnight with vemurafenib and PLX7904. Vemurafenib altered transcription of 191 mouse genes by at least 1.9-fold, while PLX7904 had minimal effects (Extended Data Fig. 2 and Supplementary Table 2). Of the genes significantly induced by vemurafenib, three encode EGFR ligands: amphiregulin, heparin-binding EGF-like growth factor, and transforming growth factor- α (TGF- α) (Extended Data Fig. 2c). The upregulation of these autocrine growth factors was confirmed at protein level and their role in potentiating the transforming potential of activated HRAS was demonstrated (Extended Data Figs 3 and 4). Induction of these ligands by vemurafenib has been demonstrated independently in vemurafenib-resistant lung cancer cell lines²⁰. All three ligands can promote cuSCC²¹. These data implicate EGFR signalling as a potential molecular link between paradoxical MAPK activation by RAF inhibitors and secondary malignancies. In contrast to vemurafenib and consistent with the paradox breaker profile, expression of the EGFR ligands was largely unaffected by PLX7904 (Extended Data Figs 2–4).

PLX7904 and a further optimized analogue PLX8394 (Fig. 1a and Table 1) are only subtly different from vemurafenib based on chemical structure. To understand how such small molecular alterations cause a drastic change in the biological profile, we obtained the crystal structure of PLX7904 in complex with BRAF^{V600E} (Extended Data Table 1). The overall binding of PLX7904 (Fig. 2a) is similar to that of vemurafenib (Extended Data Fig. 5a) with the terminal *N*-ethylmethyl group of PLX7904 occupying the same small interior pocket as the propyl group of vemurafenib. However, the methyl group of the *N*-ethylmethyl moiety forms closer contact with Leu505 in the pocket (Fig. 2b). Leu505 is one of the four residues that compose the so-called regulatory spine of kinases²² (Extended Data Fig. 6). Situated close to the carboxy (C)-terminal end of the α C helix, Leu505 is the only residue from that helix that makes direct contact with the inhibitor. RAS promotes RAF dimerization, and paradoxical MAPK pathway activation results from binding of the inhibitor to one protomer of a RAF dimer which allosterically transactivates the other protomer^{10–12}. The α C helix plays a critical role in RAF dimer formation^{10,23} and mutations that disrupt the α C helix dimer contacts counteract RAF activation by inhibitors. In an enzyme-linked immunosorbent assay (ELISA) of dimerization using cell lysates, vemurafenib and other known BRAF inhibitors promote BRAF–CRAF heterodimer formation in RAS mutant cells, whereas the dimer formation is indifferent to the presence of PLX7904 (Fig. 2c). Although the crystal structure did

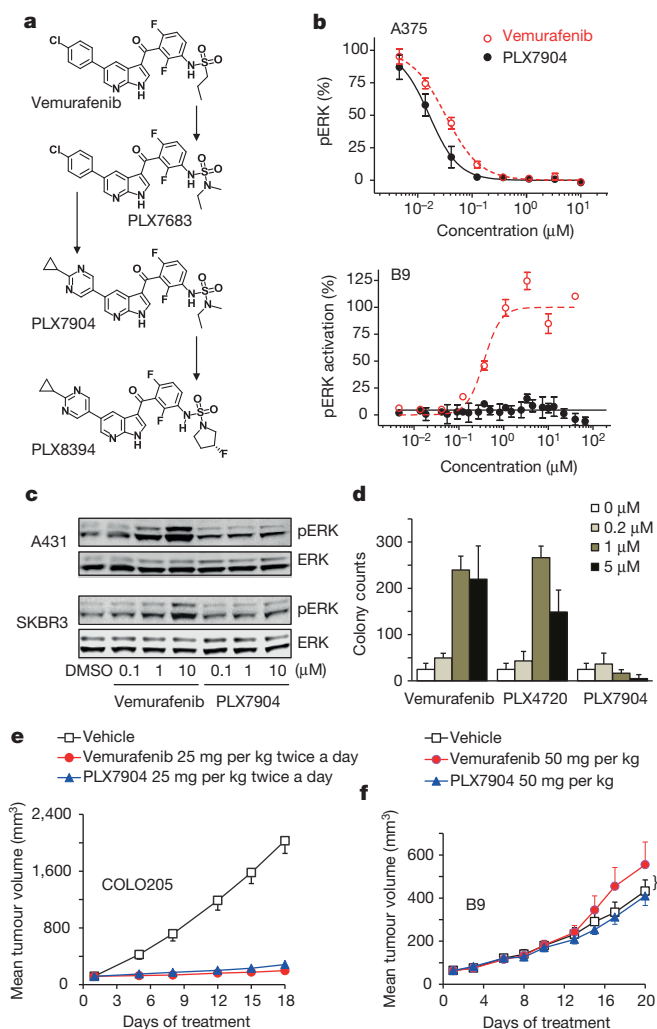


Figure 1 | Paradox breakers dissociate MAPK pathway inhibition from activation. **a**, Vemurafenib and paradox breakers PLX7683, PLX7904, and PLX8394. **b**, pERK IC₅₀ curves (mean \pm s.d.) in A375 (BRAF^{V600E}) cells and pERK EC₅₀ curves (mean \pm s.d., normalized to maximal pERK level induced by PLX4720) in B9 (HRAS^{Q61L}) cells (n = 5 experiments). **c**, pERK in A431 and SKBR3 cells after treatment for 1 h with vemurafenib or PLX7904 (full scans of western blot in Supplementary Figure 1). Repeated three times. **d**, Anchorage-independent growth of B9 cells with vemurafenib and PLX4720 (for 3 weeks) but not PLX7904 (mean \pm s.d., two experiments, three replicates each). **e**, PLX7904 and vemurafenib inhibited the COLO205 xenograft growth (mean \pm s.e.m., eight mice per group). **f**, B9 subcutaneous xenografts were stimulated by vemurafenib (* P < 0.05 by two-sided *t*-test) but not by PLX7904 (mean \pm s.e.m., ten mice per group).

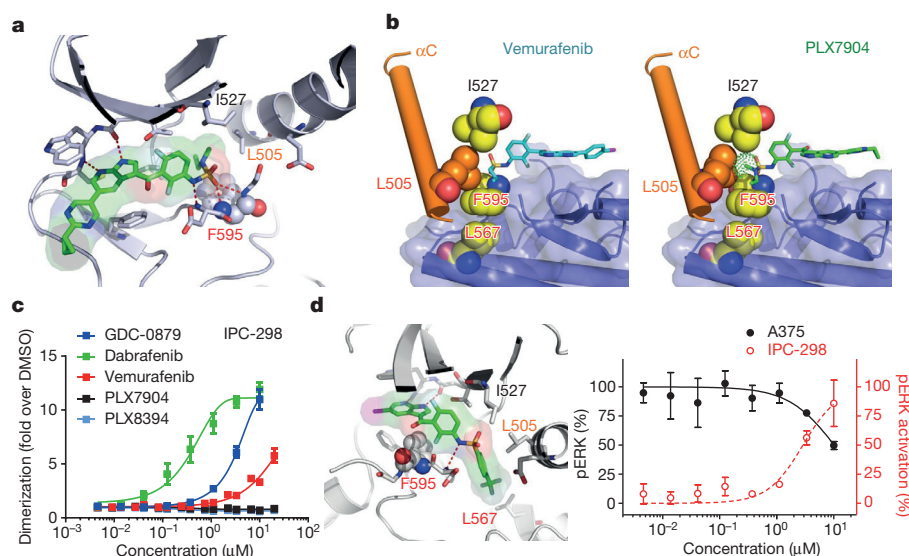


Figure 2 | Molecular mechanisms of paradox breakers. **a**, Interactions between PLX7904 (green) and BRAF^{V600E} (grey). Phe595 (spheres) shows the DFG-in (or type 1) conformation. Red dashed lines represent hydrogen bonds. **b**, The propyl-sulfonamide tail of vemurafenib (cyan) and the N-ethylmethyl-sulfamide tail of PLX7904 (green) viewed from the dimer interface. Four residues (Ile527, Leu505, Phe595, and Leu567) form the R-spine (see Extended Data Fig. 6 for definition). A dotted surface around the N-methyl group in PLX7904 illustrates its close contact with Leu505 from the α C helix (orange). **c**, BRAF–CRAF heterodimer formation in IPC-298 cells with increasing concentrations of RAF inhibitors (treatment for 1 h; mean \pm s.d., $n = 5$ experiments). **d**, Type 2 (that is, DFG-out) binder PLX5568 is a CRAF-selective inhibitor with inverse EPII (mean \pm s.d., $n = 5$ experiments).

not reveal further displacement of the α C helix by PLX7904 (Extended Data Fig. 5c), compared with the vemurafenib-bound structure the three terminal atoms (C γ , C δ 1, C δ 2) of Leu505 shifted by 0.6–1 Å to accommodate PLX7904 (Extended Data Fig. 5d). Leu505 has a higher side-chain crystallographic temperature factor (B -factor = 75) than the same residue in the vemurafenib structure (B -factor = 33). In solution where the protein is free of the artificial constraints of crystal, the strong interaction between PLX7904 and Leu505 could lead to outward movement of the α C helix, causing disruption to the RAF dimer interface. The vemurafenib-resistant L505H BRAF mutant remained sensitive to PLX7904 (ref. 24), supporting the key role played by residue 505 in sensing the structural difference between paradox breakers and first-generation RAF inhibitors.

The crystal structure of PLX4720 in complex with wild-type BRAF showed that the compound adopts a type 2 kinase inhibitor binding pose when accessing the inactive conformation of the kinase, the preferred state of wild-type RAF proteins²⁵. A PLX4720 analogue, PLX5568, made to enforce the type 2 binding orientation (Fig. 2d), has intrinsic selectivity towards CRAF (Table 1). Like other type 2 RAF inhibitors such as sorafenib, PLX5568 showed marginal inhibitory activity against BRAF^{V600E} cells but still paradoxically activated

pERK in mutant RAS cells, thus exhibiting inverse EPII (Table 1 and Fig. 2d). These data highlight the existence of a strong correlation between conformation-specific inhibition and biological outcome.

A newly discovered²⁶ and potentially common²⁷ mechanism whereby BRAF^{V600E} melanomas develop resistance to BRAF inhibition is to express aberrantly spliced forms of BRAF^{V600E} that can dimerize in the absence of activated RAS. Wild-type BRAF can be activated in a similar manner when a chromosomal translocation event results in a truncated C-terminal fragment of BRAF embedded in a fusion gene with oncogenic activity (Supplementary Table 3 and references therein). The fusion kinase, like the spliced forms of BRAF^{V600E}, dimerizes and has constitutive kinase activity and intrinsic resistance to first-generation RAF inhibitors. To test whether the paradox breaker strategy can be exploited to combat dimerization-mediated resistance, we compared the activity with PLX7904 in the SK-MEL-239 parental cell line and a representative vemurafenib-resistant clone (C3) expressing a truncated BRAF^{V600E}. PLX7904 demonstrated minimal shift in pMEK IC₅₀ and modest increase in growth inhibition IC₅₀ in C3 cells (Extended Data Fig. 7). Furthermore, both PLX7904 (that is, PB04) and PLX8394 (that is, PB03) overcame RAF inhibitor resistance in BRAF fusions characterizing paediatric astrocytomas²⁸ and maintained

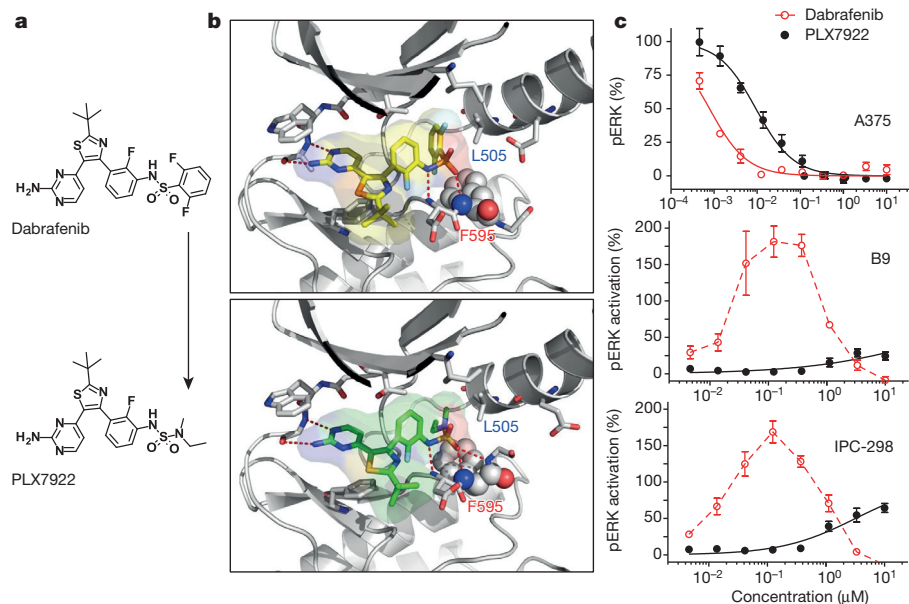


Figure 3 | The structural determinant of paradox breakers can be transferred to another chemical series to drastically alter its biological profile.

a, Substituting the 2,6-difluoro-phenylsulfonamide of dabrafenib with an N-ethylmethyl-sulfamide tail yielded PLX7922. **b**, Crystal structures of dabrafenib and PLX7922 in complex with BRAF^{V600E}. **c**, Dabrafenib (red), a highly potent inhibitor of pERK in BRAF^{V600E} cell lines, exhibited an unusual bell-shaped pERK activation curve in mutant NRAS cell lines (B9 and IPC-298). PLX7922 (black) shows markedly reduced pERK activation in mutant RAS cells with only moderately decreased pERK IC₅₀ in BRAF^{V600E} cells (A375). Mean \pm s.d. in **c**, $n = 5$ experiments.

activity against cells that are vemurafenib-resistant through secondary mutation in NRAS²⁹.

The discovery of paradox breakers confirms that the two opposing modes of action of RAF inhibitors, either blocking or activating the MAPK pathway, can be uncoupled. Since the tail moiety is primarily responsible for this uncoupling, we engineered the PLX7904 tail onto the dabrafenib scaffold (Fig. 3a, b). The resulting compound, PLX7922, showed significantly increased EPII (Fig. 3c and Table 1). Thus, the structural and chemical principles of paradox breaking can be applied to improve the safety and biological profile of other RAF inhibitors.

An alternative strategy to overcome paradoxical activation is to completely block all RAF isoforms (pan-RAF inhibition), thus severing the link between RAS and MEK/ERK. AZ-628, the first compound in this class, did show reduced (rather than induced) pERK/pMEK in RAS mutant cells, but possesses unfavourable pharmaceutical properties¹⁰. Recently, new pan-RAF inhibitors with ancillary activity on upstream SRC family kinases have been reported³⁰. The concern for pan-RAF inhibitors is that blocking MAPK signalling in normal tissue will cause toxicity. Thus, paradox breakers should afford a higher therapeutic index than the first-generation RAF inhibitors and pan-RAF inhibitors.

Online Content Methods, along with any additional Extended Data display items and Source Data, are available in the online version of the paper; references unique to these sections appear only in the online paper.

Received 24 January 2014; accepted 28 July 2015.

Published online 14 October 2015.

- Davies, H. *et al.* Mutations of the BRAF gene in human cancer. *Nature* **417**, 949–954 (2002).
- Flaherty, K. T. *et al.* Inhibition of mutated, activated BRAF in metastatic melanoma. *N. Engl. J. Med.* **363**, 809–819 (2010).
- Chapman, P. B. *et al.* Improved survival with vemurafenib in melanoma with BRAF V600E mutation. *N. Engl. J. Med.* **364**, 2507–2516 (2011).
- Sosman, J. A. *et al.* Survival in BRAF V600-mutant advanced melanoma treated with vemurafenib. *N. Engl. J. Med.* **366**, 707–714 (2012).
- Hauschild, A. *et al.* Dabrafenib in BRAF-mutated metastatic melanoma: a multicentre, open-label, phase 3 randomised controlled trial. *Lancet* **380**, 358–365 (2012).
- Su, F. *et al.* RAS mutations in cutaneous squamous-cell carcinomas in patients treated with BRAF inhibitors. *N. Engl. J. Med.* **366**, 207–215 (2012).
- Zimmer, L. *et al.* Atypical melanocytic proliferations and new primary melanomas in patients with advanced melanoma undergoing selective BRAF inhibition. *J. Clin. Oncol.* **30**, 2375–2383 (2012).
- Callahan, M. K. *et al.* Progression of RAS-mutant leukemia during RAF inhibitor treatment. *N. Engl. J. Med.* **367**, 2316–2321 (2012).
- Andrews, M. C. *et al.* BRAF inhibitor-driven tumor proliferation in a KRAS-mutated colon carcinoma is not overcome by MEK1/2 inhibition. *J. Clin. Oncol.* **31**, e448–e451 (2013).
- Hatzivassiliou, G. *et al.* RAF inhibitors prime wild-type RAF to activate the MAPK pathway and enhance growth. *Nature* **464**, 431–435 (2010).
- Heidorn, S. J. *et al.* Kinase-dead BRAF and oncogenic RAS cooperate to drive tumor progression through CRAF. *Cell* **140**, 209–221 (2010).
- Poulikakos, P. I., Zhang, C., Bollag, G., Shokat, K. M. & Rosen, N. RAF inhibitors transactivate RAF dimers and ERK signalling in cells with wild-type BRAF. *Nature* **464**, 427–430 (2010).
- Bollag, G. *et al.* Clinical efficacy of a RAF inhibitor needs broad target blockade in BRAF-mutant melanoma. *Nature* **467**, 596–599 (2010).
- King, A. J. *et al.* Dabrafenib; preclinical characterization, increased efficacy when combined with trametinib, while BRAF/MEK tool combination reduced skin lesions. *PLoS One* **8**, e67583 (2013).
- Anforth, R. M. *et al.* Cutaneous manifestations of dabrafenib (GSK2118436): a selective inhibitor of mutant BRAF in patients with metastatic melanoma. *Br. J. Dermatol.* **167**, 1153–1160 (2012).
- Oberholzer, P. A. *et al.* RAS mutations are associated with the development of cutaneous squamous cell tumors in patients treated with RAF inhibitors. *J. Clin. Oncol.* **30**, 316–321 (2012).
- Larkin, J. *et al.* Combined vemurafenib and cobimetinib in BRAF-mutated melanoma. *N. Engl. J. Med.* **371**, 1867–1876 (2014).
- Robert, C. *et al.* Improved overall survival in melanoma with combined dabrafenib and trametinib. *N. Engl. J. Med.* **372**, 30–39 (2015).
- Balmain, A., Ramsden, M., Bowden, G. T. & Smith, J. Activation of the mouse cellular Harvey-ras gene in chemically induced benign skin papillomas. *Nature* **307**, 658–660 (1984).
- Lin, L. *et al.* Mapping the molecular determinants of BRAF oncogene dependence in human lung cancer. *Proc. Natl Acad. Sci. USA* **111**, E748–E757 (2014).
- Oshima, G. *et al.* Autocrine epidermal growth factor receptor ligand production and cetuximab response in head and neck squamous cell carcinoma cell lines. *J. Cancer Res. Clin. Oncol.* **138**, 491–499 (2012).
- Taylor, S. S. & Kornev, A. P. Protein kinases: evolution of dynamic regulatory proteins. *Trends Biochem. Sci.* **36**, 65–77 (2011).
- Freeman, A. K., Ritt, D. A. & Morrison, D. K. Effects of Raf dimerization and its inhibition on normal and disease-associated Raf signaling. *Mol. Cell* **49**, 751–758 (2013).
- Choi, J. *et al.* Identification of PLX4032-resistance mechanisms and implications for novel RAF inhibitors. *Pigment Cell Melanoma Res.* **27**, 253–262 (2014).
- Tsai, J. *et al.* Discovery of a selective inhibitor of oncogenic B-Raf kinase with potent antimelanoma activity. *Proc. Natl Acad. Sci. USA* **105**, 3041–3046 (2008).
- Poulikakos, P. I. *et al.* RAF inhibitor resistance is mediated by dimerization of aberrantly spliced BRAF(V600E). *Nature* **480**, 387–390 (2011).
- Rizos, H. *et al.* BRAF inhibitor resistance mechanisms in metastatic melanoma: spectrum and clinical impact. *Clin. Cancer Res.* **20**, 1965–1977 (2014).
- Sievert, A. J. *et al.* Paradoxical activation and RAF inhibitor resistance of BRAF protein kinase fusions characterizing pediatric astrocytomas. *Proc. Natl Acad. Sci. USA* **110**, 5957–5962 (2013).
- Le, K., Blomain, E. S., Rodeck, U. & Aplin, A. E. Selective RAF inhibitor impairs ERK1/2 phosphorylation and growth in mutant NRAS, vemurafenib-resistant melanoma cells. *Pigment Cell Melanoma Res.* **26**, 509–517 (2013).
- Girotti, M. R. *et al.* Paradox-breaking RAF inhibitors that also target SRC are effective in drug-resistant BRAF mutant melanoma. *Cancer Cell* **27**, 85–96 (2015).

Supplementary Information is available in the online version of the paper.

Acknowledgements X-ray diffraction data were collected at beamline ALS 8.3.1 at the Advanced Light Source (Lawrence Berkeley National Laboratory) and the Stanford Synchrotron Radiation Lightsource (a directorate of the SLAC National Accelerator Laboratory).

Author Contributions C.Z., P.H., and G.B. designed the study and analysed data; W.S., J.Z., J.L., H. Cho, G.W., S.S., P.W., and M.N. designed and synthesized compounds, C.Z., Y.Z., T.E., and P.N.I. contributed to compound design, and G.T. and D.F. crystallized and collected data; Y.Z. and W.W. processed and refined X-ray data; E.A.B., Y.M., G.H., and B.M. performed assays; A.M., E.L., L.S., G.V., H.R., and P.N.I. performed absorption, distribution, metabolism, and excretion (ADME) and toxicity assays and formulation; H.N. conducted cloning and microarray experiments; R.S., H. Carias, and B.P. purified proteins; G.H., J.T., and B.W. assisted in pharmacology study design; J.W. managed compound inventory and plating; P.S.L., K.N., and P.N.I. were involved in overall study design; C.Z. and G.B. wrote the paper with input from the other authors.

Author Information Atomic coordinates and structure factors have been deposited in the Protein Data Bank under accession numbers 4XV1 (BRAF^{V600E}-PLX7904), 4XV9 (BRAF^{WT}-PLX5568), 4XV3 (BRAF^{V600E}-PLX7922) and 4XV2 (BRAF^{V600E}-dabrafenib). Microarray data have been deposited in the NCBI Gene Expression Omnibus under accession number GSE71109. Reprints and permissions information is available at www.nature.com/reprints. The authors declare competing financial interests: details are available in the online version of the paper. Readers are welcome to comment on the online version of the paper. Correspondence and requests for materials should be addressed to G.B. (gbollag@plexikon.com) or C.Z. (czhang@plexikon.com).

METHODS

With the exception of tumour xenograft studies, no statistical methods were used to predetermine sample size. The experiments were not randomized. The investigators were not blinded to allocation during experiments and outcome assessment.

Generation of BRAF small molecule inhibitors. All solvents and reagents were used as obtained from commercial sources. Starting materials were purchased from commercial sources or prepared according to methods reported in the literature. Reactions involving air- or moisture-sensitive reagents were performed under a nitrogen atmosphere. NMR spectra were recorded in deuterated solvent with an Agilent 400 MHz MR DD2 spectrometer system equipped with an Oxford AS400 magnet. Chemical shifts are expressed as δ units and referenced to the residual ^1H or ^{13}C solvent signal. All coupling constants (J) are reported in hertz (s, singlet; d, doublet; t, triplet; q, quartet; m, multiplet; br, broad peak; dd, doublet of doublets; ddd, doublet of doublet of doublets; dm, doublet of multiplets). Mass spectra were measured with a Shimadzu LCMS-2020 spectrometer coupled to a Shimadzu 20A high-performance liquid chromatography (HPLC) system operating in reverse mode. Analytical purity was greater than 95% for final compounds and was determined using the following HPLC method. Buffer A: 5% acetonitrile, 95% water, 0.01% formic acid; buffer B: 95% CH_3CN , 5% water, 0.01% formic acid; Siliachrom XDB C18, 5 μm , 2.1×50 mm, 5–95% B in 6 min, 1.0 ml min^{-1} , 220 nm and 254 nm, electrospray-ionization-positive (ESI-positive), 300–800 atomic mass units.

(2,6-Difluoro-3-nitrophenyl)(5-iodo-1*H*-pyrrolo[2,3-*b*]pyridin-3-yl)methanone. 5-Iodo-1*H*-pyrrolo[2,3-*b*]pyridine (160 g, 0.656 mol) and aluminium chloride (525 g, 3.94 mol) in nitromethane (1,640 ml) were allowed to stir at room temperature (20–25 °C) for 1 h. Then 2,6-difluoro-3-nitrobenzoyl chloride (218 g, 0.984 mmol) in nitromethane (1,640 ml) was added and the mixture was heated at 50 °C for 4 days. After cooling to 0 °C, the reaction was quenched with the dropwise addition of methanol (1.5 l), resulting in a precipitate. The mixture was diluted with water (2 l) and filtered. The crude product was triturated with methyl *tert*-butyl ether and filtered to give the title compound as a tan solid which was used directly in the next step (281 g, theory) without further purification. ^1H NMR (400 MHz, dimethylsulfoxide ($\text{DMSO}-d_6$)) 13.18 (br s, 1 H), 8.82 (s, 1 H), 8.62 (s, 1 H), 8.46 (m, 1 H), 8.40 (s, 1 H), 7.55 (m, 1 H).

(3-Amino-2,6-difluorophenyl)(5-iodo-1*H*-pyrrolo[2,3-*b*]pyridin-3-yl)methanone. To (2,6-difluoro-3-nitrophenyl)(5-iodo-1*H*-pyrrolo[2,3-*b*]pyridin-3-yl)methanone (281 g, 656 mmol) in ethyl acetate (10.9 l) and tetrahydrofuran (10.9 l) was added tin(II) chloride dihydrate (517 g, 2.29 mol) portionwise while heating at 60 °C. The reaction mixture was held at this temperature overnight. After cooling to room temperature, the reaction mixture was quenched with 50% saturated aqueous sodium bicarbonate (1:1 water and saturated aqueous sodium bicarbonate) and filtered through Celite washing the cake with ethyl acetate. The layers were separated and the organic layer was washed with brine and then concentrated under reduced pressure to give the crude product, which was triturated with methyl *tert*-butyl ether and filtered to give the title compound as a tan solid (216 g, 541 mmol, 83% yield). ^1H NMR (400 MHz, $\text{DMSO}-d_6$) 12.96 (br s, 1 H), 8.72 (s, 1 H), 8.56 (d, $J = 2.0$ Hz, 1 H), 8.06 (s, 1 H), 6.92 (dd, $J = 8.6$ Hz, 1 H), 6.88 (m, 1 H), 5.20 (s, 2 H); liquid chromatography–mass spectrometry (LC/MS) (ESI-positive) m/z : 399.9 ($\text{M} + \text{H}^+$).

(3-Amino-2,6-difluorophenyl)(5-(2-cyclopropylpyrimidin-5-yl)-1*H*-pyrrolo[2,3-*b*]pyridin-3-yl)methanone. A mixture of (3-amino-2,6-difluorophenyl)(5-iodo-1*H*-pyrrolo[2,3-*b*]pyridin-3-yl)methanone (93 g, 233 mmol), 2-cyclopropyl-5-(4,4,5,5-tetramethyl-1,3,2-dioxaborolan-2-yl)pyrimidine (229 g, 466 mmol, ~50% purity), potassium carbonate (97.0 g, 702 mmol), and [1,1'-bis(diphenylphosphino)ferrocene]dichloropalladium(II) dichloromethane complex (19.0 g, 23.3 mmol) in dioxane (930 ml) and water (465 ml) was heated at 100 °C for several hours. Upon cooling, the reaction mixture was diluted with water and extracted with a mixture of tetrahydrofuran and ethyl acetate. The organic layer was separated and concentrated under reduced pressure to give the crude product, which was triturated with dichloromethane/methyl *tert*-butyl ether and filtered, washing with methyl *tert*-butyl ether to give the title compound as a tan solid (71.0 g, 78% yield). ^1H NMR (400 MHz, $\text{DMSO}-d_6$) 12.95 (br s, 1 H), 9.07 (s, 2 H), 8.71 (d, $J = 2.3$ Hz, 1 H), 8.66 (s, 1 H), 8.11 (s, 1 H), 6.92 (dd, $J = 9.0$ Hz, 9.0 Hz, 1 H), 6.89 (ddd, $J = 5.9$ Hz, 9.0 Hz, 9.0 Hz, 1 H), 5.20 (s, 2 H), 2.27 (m, 1 H), 1.03–1.22 (m, 4 H); LC/MS (ESI-positive) m/z : 392.2 ($\text{M} + \text{H}^+$).

5-(2-Cyclopropylpyrimidin-5-yl)-3-[3-[[ethyl(methyl)sulfamoyl]amino]-2,6-difluoro-benzoyl]-1*H*-pyrrolo[2,3-*b*]pyridine (PLX7904). To (3-amino-2,6-difluorophenyl)(5-(2-cyclopropylpyrimidin-5-yl)-1*H*-pyrrolo[2,3-*b*]pyridin-3-yl)methanone (53.8 g, 138 mmol) in pyridine (1375 ml) was added ethyl(methyl)sulfamoyl chloride (65.0 g, 412 mmol) and the reaction was heated at 65 °C overnight. The volatiles were removed under reduced pressure and the residue was partitioned between water and ethyl acetate/tetrahydrofuran. The organic layer was

concentrated under reduced pressure to give the crude product, which was dry loaded onto silica gel and purified by silica gel column chromatography (twice) eluting with 0–10% methanol/dichloromethane, then purified by silica gel column chromatography eluting with ethyl acetate. The fractions containing the desired product were pooled and concentrated under reduced pressure. The resulting solid was triturated with methyl *tert*-butyl ether and filtered to give the title compound as a white solid (21.1 g, 30% yield). ^1H NMR (400 MHz, $\text{DMSO}-d_6$) 13.07 (br s, 1 H), 9.71 (br s, 1 H), 9.03 (s, 2 H), 8.76 (s, 1 H), 8.68 (s, 1 H), 8.19 (s, 1 H), 7.59 (ddd, $J = 5.9$ Hz, 9.0 Hz, 9.0 Hz, 1 H), 7.27 (dd, $J = 9.0$ Hz, 9.0 Hz, 1 H), 3.12 (q, $J = 7.0$ Hz, 2 H), 2.74 (s, 3 H), 2.29 (m, 1 H), 1.03–1.22 (m, 4 H), 0.95 (t, $J = 7.0$ Hz, 3 H); ^{13}C NMR (100 MHz, $\text{DMSO}-d_6$) 181.1, 170.4, 156.1 (dd, $J_{\text{CF}} = 246$ Hz, $J_{\text{CF}} = 6.9$ Hz), 155.5, 152.4 (dd, $J_{\text{CF}} = 250$ Hz, $J_{\text{CF}} = 8.4$ Hz), 149.7, 144.3, 139.2, 128.9, 128.6 (d, $J_{\text{CF}} = 9.9$ Hz), 127.7, 126.2, 123.0 (dd, $J_{\text{CF}} = 13.3$ Hz, $J_{\text{CF}} = 3.4$ Hz), 118.5 (dd, $J_{\text{CF}} = 24.6$ Hz, $J_{\text{CF}} = 22.5$ Hz), 117.9, 116.2, 112.7 (dd, $J_{\text{CF}} = 22.5$ Hz, $J_{\text{CF}} = 3.4$ Hz), 45.3, 34.4, 18.2, 13.3, 10.9; LC/MS (ESI-positive) m/z : 513.3 ($\text{M} + \text{H}^+$).

(3*R*)-*N*-[3-[5-(2-cyclopropylpyrimidin-5-yl)-1*H*-pyrrolo[2,3-*b*]pyridine-3-carbonyl]-2,4-difluoro-phenyl]-3-fluoro-pyrrolidine-1-sulfonamide (PLX8394). This material was prepared in a manner analogous to PLX7904 using (3*R*)-3-fluoropyrrolidine-1-sulfonyl chloride in place of ethyl(methyl)sulfamoyl chloride. The product was purified by reverse-phase HPLC to provide, after lyophilization, the title compound as a white solid. ^1H NMR (400 MHz, $\text{DMSO}-d_6$) 13.05 (br s, 1 H), 9.84 (br s, 1 H), 9.01 (s, 2 H), 8.73 (s, 1 H), 8.67 (s, 1 H), 8.15 (s, 1 H), 7.62 (ddd, $J = 5.9$ Hz, 9.0 Hz, 9.0 Hz, 1 H), 7.26 (dd, $J = 9.0$ Hz, 9.0 Hz, 1 H), 5.29 (dm, $J = 51.6$ Hz (H-F), 1 H), 3.43 (dm, 2 H), 3.33 (m, 2 H), 2.27 (m, 1 H), 2.04 (m, 2 H), 1.01–1.11 (m, 4 H); ^{13}C NMR (100 MHz, $\text{DMSO}-d_6$) 181.1, 170.4, 156.2 (dd, $J_{\text{CF}} = 247$ Hz, $J_{\text{CF}} = 6.9$ Hz), 155.5, 152.6 (dd, $J_{\text{CF}} = 249$ Hz, $J_{\text{CF}} = 8.4$ Hz), 149.7, 144.3, 139.2, 128.9, 128.7 (d, $J_{\text{CF}} = 9.2$ Hz), 127.7, 126.2, 122.9 (dd, $J_{\text{CF}} = 13.7$ Hz, $J_{\text{CF}} = 3.8$ Hz), 118.5 (dd, $J_{\text{CF}} = 24.4$ Hz, $J_{\text{CF}} = 22.2$ Hz), 117.9, 116.2, 112.7 (dd, $J_{\text{CF}} = 22.9$ Hz, $J_{\text{CF}} = 3.9$ Hz), 93.4 (d, $J_{\text{CF}} = 175$ Hz), 54.9 (d, $J_{\text{CF}} = 22.9$ Hz), 46.5, 32.5 (d, $J_{\text{CF}} = 21.3$ Hz), 18.2, 10.9; LC/MS (ESI-positive) m/z : 542.9 ($\text{M} + \text{H}^+$).

2-*Tert*-butyl-5-(2-chloropyrimidin-4-yl)-4-[3-[[ethyl(methyl)sulfamoyl]amino]-2-fluoro-phenyl]thiazole. To a solution of 3-[2-*tert*-butyl-5-(2-chloropyrimidin-4-yl)thiazol-4-yl]-2-fluoroaniline (102 mg, 0.281 mmol) in dichloromethane (1 ml) was added pyridine (0.5 ml) followed by ethyl(methyl)sulfamoyl chloride (265 mg, 1.68 mmol). The reaction was allowed to stir at 50 °C for 96 h. The reaction was worked up by extraction with ethyl acetate and 0.1 M HCl (aq). The product was purified by flash chromatography (5–30% ethyl acetate in hexanes) which gave impure material. This material was again purified by flash chromatography (0.5–6% methanol in dichloromethane). This provided the title compound (55 mg, 41% yield), which was used in the next step. ^1H NMR (400 MHz, CD_3CN) 8.45 (d, $J = 5.4$ Hz, 1 H), 7.66 (t, $J = 7.5$ Hz, 1 H), 7.55 (s, 1 H), 7.38 (t, $J = 7.5$ Hz, 1 H), 7.34 (dd, $J = 8.0$ Hz, 1 H), 7.04 (d, $J = 5.4$ Hz, 1 H), 3.19 (q, $J = 7.2$ Hz, 2 H), 2.79 (s, 3H), 1.51 (s, 9 H), 1.09 (t, $J = 7.3$ Hz, 3 H); LC/MS (ESI-positive) m/z : 484.2 ($\text{M} + \text{H}^+$).

5-(2-Aminopyrimidin-4-yl)-2-*tert*-butyl-4-[3-[[ethyl(methyl)sulfamoyl]amino]-2-fluoro-phenyl]thiazole (PLX7922). A solution of 2-*tert*-butyl-5-(2-chloropyrimidin-4-yl)-4-[3-[[ethyl(methyl)sulfamoyl]amino]-2-fluoro-phenyl]thiazole (51 mg, 0.11 mmol) dissolved in 5 ml of 7 M ammonia in methanol in a sealed reaction vial was placed in an oil bath at 80 °C and allowed to stir. After 48 h, the reaction was concentrated under reduced pressure and the resulting residue was purified by reverse-phase HPLC to provide the title compound, after lyophilization, as a white solid (31 mg, 61% yield). ^1H NMR (400 MHz, $\text{DMSO}-d_6$) 9.71 (br s, 1 H), 8.04 (d, $J = 5.1$ Hz, 1 H), 7.54 (m, 1 H), 7.30 (m, 2 H), 6.77 (br s, 2 H), 6.03 (d, $J = 5.1$ Hz, 1 H), 3.06 (q, $J = 7.0$ Hz, 2 H), 2.67 (s, 3 H), 1.41 (s, 9 H), 0.99 (t, $J = 7.0$ Hz, 3 H); ^{13}C NMR (100 MHz, $\text{DMSO}-d_6$) 181.9, 163.9, 159.3, 158.1, 152.2 (d, $J_{\text{CF}} = 251$ Hz), 145.9, 134.7, 127.8, 126.9 (d, $J_{\text{CF}} = 13$ Hz), 126.5, 125.2 (d, $J_{\text{CF}} = 5$ Hz), 124.3 (d, $J_{\text{CF}} = 14.7$ Hz), 105.8, 45.3, 38.1, 34.5, 30.8, 13.2; LC/MS (ESI-positive) m/z : 465.2 ($\text{M} + \text{H}^+$).

N-[3-[[5-(chloro-1*H*-pyrrolo[2,3-*b*]pyridin-3-yl)-hydroxy-methyl]-2,4-difluoro-phenyl]-4-(trifluoromethyl)benzenesulfonamide. To a solution of *N*-(2,4-difluoro-3-formyl-phenyl)-4-(trifluoromethyl)benzenesulfonamide (83.4 g, 0.228 mol) and 5-chloro-1*H*-pyrrolo[2,3-*b*]pyridine (34.8 g, 0.228 mol) in anhydrous methanol (350 ml) was added potassium hydroxide (38.4 g, 0.684 mol). The reaction mixture was stirred at room temperature, under nitrogen, for 3 h and poured into water (1 l). The product was extracted with ethyl acetate (2 \times 800 ml). The organic layers were combined, washed with brine (800 ml), dried, and concentrated under reduced pressure to yield a brown solid. This solid was suspended in acetonitrile (10 vol) overnight with stirring and then cooled in an ice bath for 3 h. The solids were isolated by filtration, washed with a minimum of cold acetonitrile, and dried to provide the title compound (56.8 g, 48% yield). ^1H NMR (400 MHz, $\text{DMSO}-d_6$) 11.77 (s, 1 H), 10.38 (s, 1 H), 8.17 (d, $J = 2.3$ Hz, 1 H), 7.88 (s, 4 H), 7.75 (d, $J = 2.3$ Hz, 1 H), 7.18 (s, 1 H), 7.17 (m, 1 H), 7.05 (t, $J = 9.0$ Hz, 1 H), 6.20 (d, $J = 4.9$ Hz, 1 H), 6.02 (d, $J = 4.9$ Hz, 1 H); LC/MS (ESI-positive) m/z : 518.0 ($\text{M} + \text{H}^+$).

N-[3-(5-chloro-1*H*-pyrrolo[2,3-*b*]pyridine-3-carbonyl)-2,4-difluoro-phenyl]-4-(trifluoromethyl)benzenesulfonamide (PLX5568). To a solution of *N*-[3-[(5-chloro-1*H*-pyrrolo[2,3-*b*]pyridin-3-yl)-hydroxy-methyl]-2,4-difluoro-phenyl]-4-(trifluoromethyl)benzenesulfonamide (100 g, 0.193 mol) in tetrahydrofuran (2.5 l) was added to Dess–Martin periodinane (99.2 g, 0.234 mol) under nitrogen. When the reaction was complete, the mixture was poured into 1 M sodium thiosulfate (700 ml) and saturated sodium bicarbonate solution (700 ml) and then extracted with ethyl acetate (2 × 700 ml). The organic layers were combined, washed with brine (800 ml), dried, and concentrated under reduced pressure to yield a brown solid. This residue was stirred in ethyl acetate (1 l) and silica (100 g) for 45 min and diluted with hexane (500 ml). The mixture was poured through a plug of silica and the product was eluted with 50:50 hexane:ethyl acetate. The fractions containing the product were combined and concentrated under reduced pressure to yield crude product as a yellow solid. Recrystallization of the crude product from ethanol provided the title compound as a pale yellow solid (71 g, 71% yield). ¹H NMR (400 MHz, DMSO-*d*₆) 13.13 (s, 1 H), 10.51 (s, 1 H), 8.43 (s, 1 H), 8.38 (d, *J* = 2.4 Hz, 1 H), 8.18 (d, *J* = 2.4 Hz, 1 H), 7.93 (s, 4 H), 7.44 (m, 1 H), 7.28 (m, 1 H); ¹³C NMR (100 MHz, DMSO-*d*₆) 180.7, 157.0 (dd, *J*_{CF} = 247 Hz, *J*_{CF} = 7.3 Hz), 153.5 (dd, *J*_{CF} = 251 Hz, *J*_{CF} = 8.4 Hz), 148.1, 144.0, 143.9, 139.9, 133.1 (q, *J*_{CF} = 32.3 Hz), 130.4 (d, *J*_{CF} = 9.2 Hz), 128.7, 128.1, 126.9 (q, *J*_{CF} = 3.8 Hz), 126.3, 123.8 (q, *J*_{CF} = 273 Hz), 121.3 (dd, *J*_{CF} = 13.8 Hz, *J*_{CF} = 3.8 Hz), 118.6, 118.4 (dd, *J*_{CF} = 25.4 Hz, *J*_{CF} = 22.6 Hz), 115.3, 113.1 (dd, *J*_{CF} = 23.1 Hz, *J*_{CF} = 3.8 Hz); (LC/MS (ESI-positive) *m/z*: 516.1 (M + H⁺)).

In vitro and in vivo studies. *Biochemical assays and kinase selectivity profiling.* The *in vitro* RAF kinase activities were determined by measuring phosphorylation of a biotinylated substrate peptide as described previously²⁵. PLX7904 was also tested against a panel of 287 kinases at concentrations of 1 μM in duplicate. Kinases inhibited by over 50% were followed up by IC₅₀ determination. The 287 kinases represent all major branches of the kinase phylogenetic tree. The inhibition screen of 287 kinases was performed under contract as complementary panels at Invitrogen (Life Technologies) SelectScreen profiling service, DiscoverX KINOMEScan service, and Reaction Biology Corporation Kinase HotSpot service. *Cell culture experiments.* The B9 cell line was a gift from A. Balmain. The SK-MEL-239 and SK-MEL-239-C3 cell lines were provided by D. Solit and N. Rosen. The IPC-298 cell line was purchased from DSMZ. All other cell lines (A375, A431, COLO29, HCT116, and SKBR3) were purchased from ATCC. All cell lines were authenticated at the source by STR profiling and tested negative for mycoplasma contamination before use. Compounds dilutions were done in 100% DMSO and these titrations were diluted 500-fold in culture medium when added to cells, resulting in a final 0.2% DMSO concentration. Final compound concentrations are listed in text and figures.

Phospho-ERK AlphaScreen assay. To determine the effects of compound treatment on phosphorylation of ERK1/2, cells were plated in a 96-well plate and treated with an eight-point titration of compound for 1 h at 37 °C before lysis. To detect pERK, cell lysates were incubated with streptavidin-coated AlphaScreen donor beads, anti-mouse IgG AlphaScreen acceptor beads, a biotinylated anti-ERK1/2 rabbit antibody, and a mouse antibody that recognized ERK1/2 only when it was phosphorylated on Thr202 and Tyr204. The biotinylated ERK1/2 antibody bound both to the streptavidin-coated AlphaScreen donor beads and to ERK1/2 (regardless of its phosphorylation state), and the phospho-ERK1/2 antibody bound to the acceptor beads and to ERK1/2 that was phosphorylated at Thr202/Tyr204. An increase in ERK1/2 phosphorylation at Thr202/Tyr204 brought the donor and acceptor AlphaScreen beads into close proximity, generating a signal that could be quantified on an EnVision reader (Perkin Elmer). Inhibition of ERK phosphorylation resulted in a loss of signal compared with DMSO controls.

Phospho-ERK immunoblot analysis. Western blots were performed by standard techniques and analysed on an Odyssey Infrared Scanner (Li-COR Biosciences). The following antibodies were used: pERK1/2 (T202/Y204) and ERK1/2 (Cell Signaling).

Growth inhibition assay. Cells were plated into a 96-well plate at a density of 3,000 cells per well and allowed to adhere overnight. Compounds were dissolved in DMSO, diluted threefold to create an eight-point titration, and added to cells. After incubation for 72 h, cell viability was examined using CellTiter-Glo (Promega).

Anchorage-independent growth assay. Twenty-five thousand B9 cells were plated in each well of a six-well plate with a bottom layer of 1% and a top layer of 0.4% low melting agar (Sigma A4018) containing RPMI 1640 medium with 10% FBS. For the RAF inhibitor study, B9 cells grown in soft agar were treated with vemurafenib, PLX4720 or PLX7904 at the indicated concentrations, or DMSO at 0.2% final concentration for 3 weeks. For the EGFR ligand study, B9 cells grown in soft agar were treated with AREG (R&D Systems 989-AR), TGF-α (R&D Systems 239-A),

or HB-EGF (R&D Systems 259-HE) at the indicated concentrations for 3 weeks. For the vemurafenib and erlotinib combination study, B9 cells grown in soft agar were treated with vemurafenib, erlotinib, or a combination of the two compounds at the indicated concentrations, or DMSO for 3 weeks. Anchorage-independent colonies ≥ 100 μm were scored using AxioVision Rel 4.8 software (Carl Zeiss).

ELISA for detecting EGFR ligands. Twenty thousand B9 cells were plated in each well of a 96-well plate and treated with DMSO control or compounds at the indicated concentrations for 48 h. Cell supernatants were collected and cells were lysed using 1 × cell lysis buffer (CST 9803). The amounts of AREG, TGF-α, and HB-EGF in cell supernatants or cell lysates were determined with the use of ELISA Development kits (R&D Systems DY989, DY239, and 259-HE-050N) according to the manufacturer's instructions.

EGFR signalling assay. B9 cells were treated with 1 μM or 5 μM vemurafenib or control vehicle for the indicated times in the absence of serum. Supernatants from treated B9 cells were then collected and added to newly plated, serum-starved (overnight) B9 cells for 10 min. Cells were washed with 1 × PBS twice, lysed, and subjected to western blot analysis. pEGFR Y1068, EGFR, pAkt S473, and Akt antibodies were purchased from Cell Signaling Technology.

RAF dimerization assays. BRAF–CRAF heterodimerization was characterized in cell lysates. Cells were plated on 96-well dishes and allowed to adhere overnight at 37 °C. Cells were treated with compound or DMSO for 1 h at 37 °C before lysis in RIPA buffer containing protease and phosphatase inhibitors. The lysates were transferred to ELISA plates coated with a monoclonal CRAF capture antibody, and incubated overnight at 4 °C. Further incubations with a polyclonal BRAF detection antibody and a horseradish-peroxidase-labelled secondary antibody were done at room temperature. After incubation with TMB substrate and sulfuric acid, the signal was analysed by measuring absorbance at 450 nm on a Tecan Safire plate reader.

Microarray gene expression analysis. B9 cells were plated in 1 μM vemurafenib, 1 μM PLX7904 or 0.2% DMSO vehicle control and incubated for 17 h. Cells were harvested, total RNA was isolated (RNeasy Mini Kit, Qiagen), and gene expression was measured using Affymetrix Mouse420_2 chips following the manufacturer's instructions. Vemurafenib response genes were identified by requiring the ratio between the treated and vehicle control samples be more than 1.9 (upregulated) or less than 0.54 (downregulated).

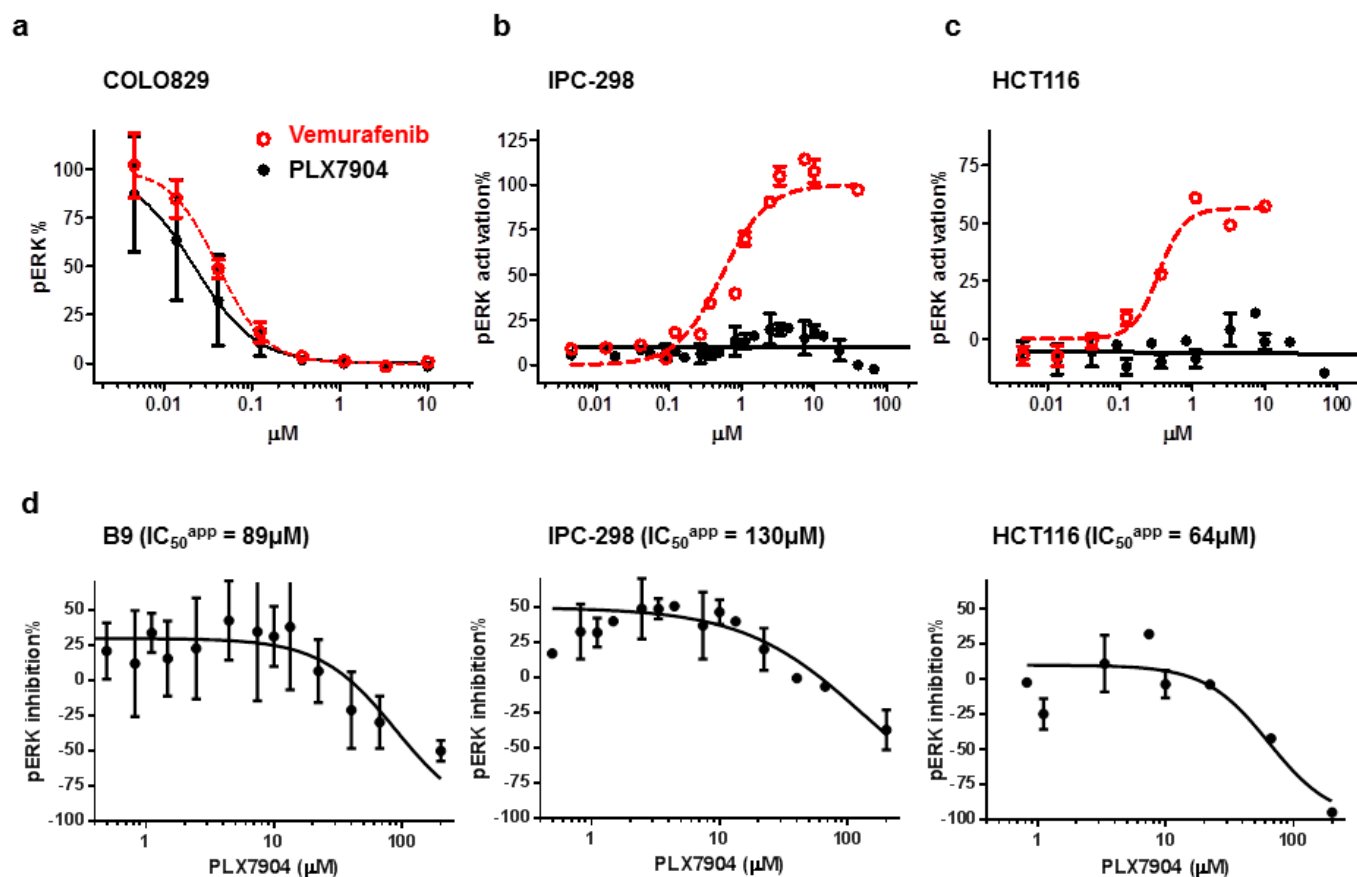
Tumour xenograft studies. All animal studies were conducted in accordance with the Institute for Laboratory Animal Research Guide for the Care and Use of Laboratory Animals and the US Department of Agriculture's Animal Welfare Act and approved by the institutional review board at testing facilities. Sample size (number of mice per group) was selected to provide at least 80% power to detect a two s.d. difference of mean tumour volume between two groups with two-sided type I error = 1%. The same formulation was used for both COLO205 and B9 xenograft studies. The powder of the test compound was dissolved in pure *N*-methyl-2-pyrrolidone. Diluent consisted of PEG400:TPGS:Poloxamer 407:water (40:5:5:50). Before gavage administration, fresh stock of *N*-methyl-2-pyrrolidone compound solution (or *N*-methyl-2-pyrrolidone for vehicle) was thoroughly mixed with the diluents to make a uniform suspension. Dosing volume was 5 μl g⁻¹. On the last day of the efficacy study, blood samples were collected at 0, 2, 4, and 8 h after last dosing, two animals per time point, for pharmacokinetic analysis. Animals were fed a standard rodent diet and water was supplied *ad libitum*. Tumour measurements were taken with an electronic microcalliper three times weekly. In addition, body weights were recorded at these times. Test facility investigators were blinded to the group allocation during the experiment.

COLO205 tumour cells were cultured in DMEM 10% FBS 1% penicillin/streptomycin supplemented with bovine insulin, at 37 °C. Balb/C nude mice, female, 6–8 weeks old, weighing approximately 18–22 g, were inoculated subcutaneously at the right flank with COLO205 tumour cells (5 × 10⁶) in 0.1 ml of PBS mixed with matrigel (50:50) for tumour development. The treatment was started when mean tumour size reached approximately 100 mm³, with eight mice in each treatment group randomized to balance the average weight and tumour size. B9 cells were expanded in DMEM 10% FBS 1% penicillin/streptomycin. Upon trypsinization the cells were washed three times with 20 ml RPMI, and after the final centrifugation were re-suspended, counted, and adjusted by volume to a final concentration of 5 × 10⁷ cells per millilitre. B9 xenografts were started by injection of 5 × 10⁶ cells subcutaneously in 6- to 7-week-old female nude Balb/c mice. Compound dosing started when the average size of tumours reached 50–70 mm³. Animals were equally distributed over treatment groups (*n* = 10) to balance the average tumour size and body weight. Animals were dosed orally for days 1–14 twice daily and days 15–28 once daily with vehicle, vemurafenib 50 mg per kg, or PLX7904 50 mg per kg. 12-*O*-tetradecanoylphorbol-13-acetate (TPA) was put on the skin of all mice twice a week during weeks 3 and 4 at a dose of 2 μg in 200 μl acetone.

Crystallization and structure determination. Expression and purification of BRAF and BRAF^{V600E} were performed as previously described^{13,25}. Crystallization drops were prepared by mixing the protein solution with 1 mM of compound and the same amount of reservoir, and drops were incubated by vapour diffusion (sitting drops) at 4 °C. The mother liquor used to obtain co-crystals of PLX7904, dabrafenib, and PLX7922 with BRAF^{V600E} consisted of 0.1 M BisTris at pH 6.0, 12.5% 2,5-hexanediol, 12% PEG3350; the reservoir used to obtain co-crystals of PLX5568 with BRAF^{WT} contained 0.1 M MES at pH 6.0, 35% (v/v) 2-methyl-2,4-pentanediol, and 0.2 M Li₂SO₄. All co-crystals were flash-frozen with liquid nitrogen, but BRAF^{V600E} co-crystals were soaked in a solution containing the mother liquor plus 20% glycerol, before flash-freezing. X-ray diffraction data were collected at beamline 8.3.1 at the Advanced Light Source (Lawrence Berkeley Laboratory) and beamline 9.1 at Stanford Synchrotron Radiation Lightsource (Stanford University). Data were processed and scaled using MOSFLM³¹ and SCALA in the CCP4 package³². All co-structures were solved using molecular replacement with the program MOLREP³³. The starting models used were the inhibitor-bound BRAF^{V600E} and BRAF^{WT}, respectively (Protein Data Bank accession numbers 4FK3 and 1UWJ). The final

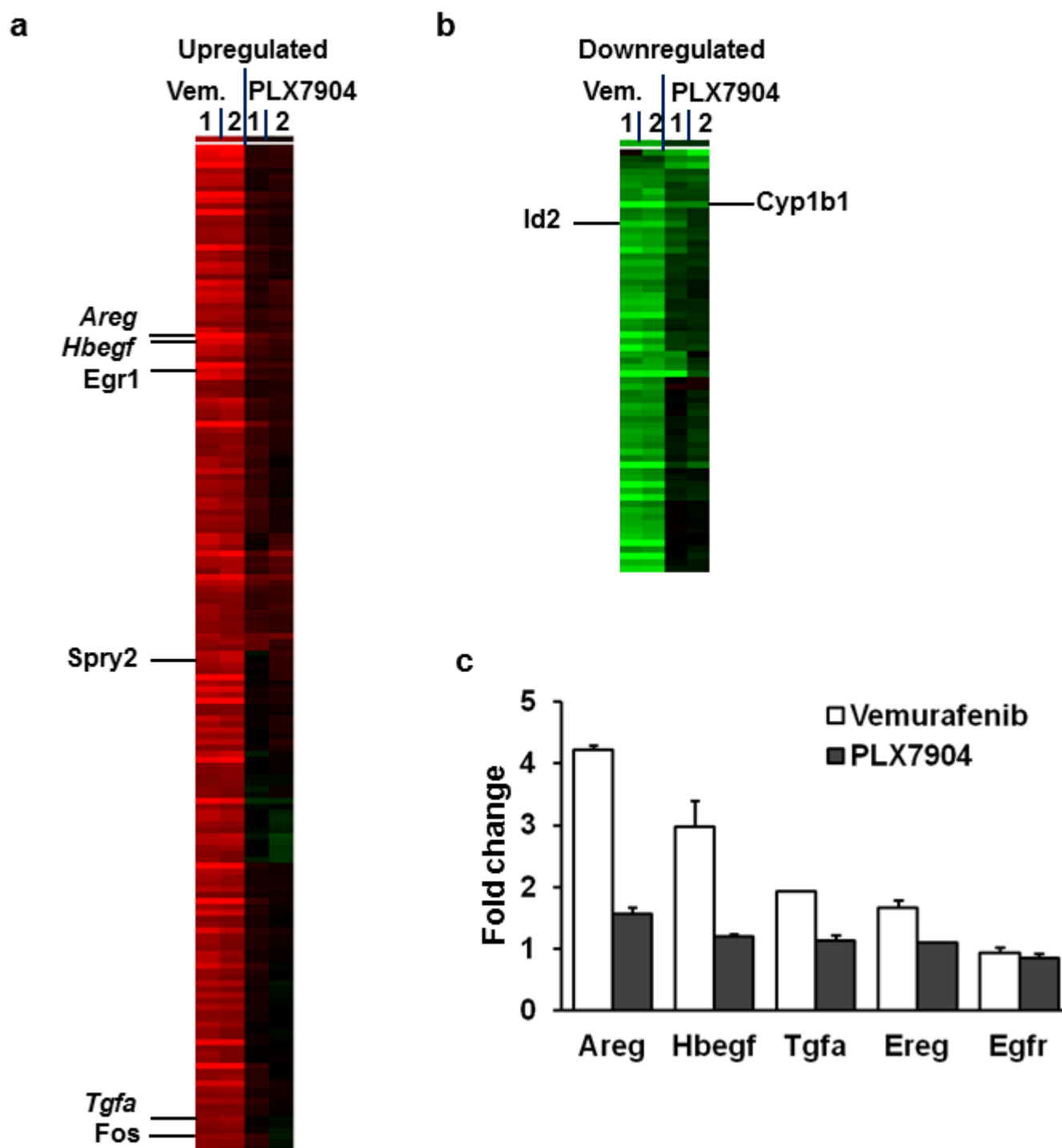
models were obtained after several rounds of manual rebuilding and refinement with PHENIX³⁴ and REFMAC³⁵. A summary of the crystallography statistics is included in Extended Data Table 1.

31. Powell, H. R. The Rossmann Fourier autoindexing algorithm in MOSFLM. *Acta Crystallogr. D* **55**, 1690–1695 (1999).
32. Winn, M. D. *et al.* Overview of the CCP4 suite and current developments. *Acta Crystallogr. D* **67**, 235–242 (2011).
33. Vagin, A. & Teplyakov, A. Molecular replacement with MOLREP. *Acta Crystallogr. D* **66**, 22–25 (2010).
34. Adams, P. D. *et al.* PHENIX: a comprehensive Python-based system for macromolecular structure solution. *Acta Crystallogr. D* **66**, 213–221 (2010).
35. Murshudov, G. N., Vagin, A. A. & Dodson, E. J. Refinement of macromolecular structures by the maximum-likelihood method. *Acta Crystallogr. D* **53**, 240–255 (1997).
36. Joseph, E. W. *et al.* The RAF inhibitor PLX4032 inhibits ERK signalling and tumor cell proliferation in a V600E BRAF-selective manner. *Proc Natl Acad Sci USA* **107**, 14903–14908 (2010).



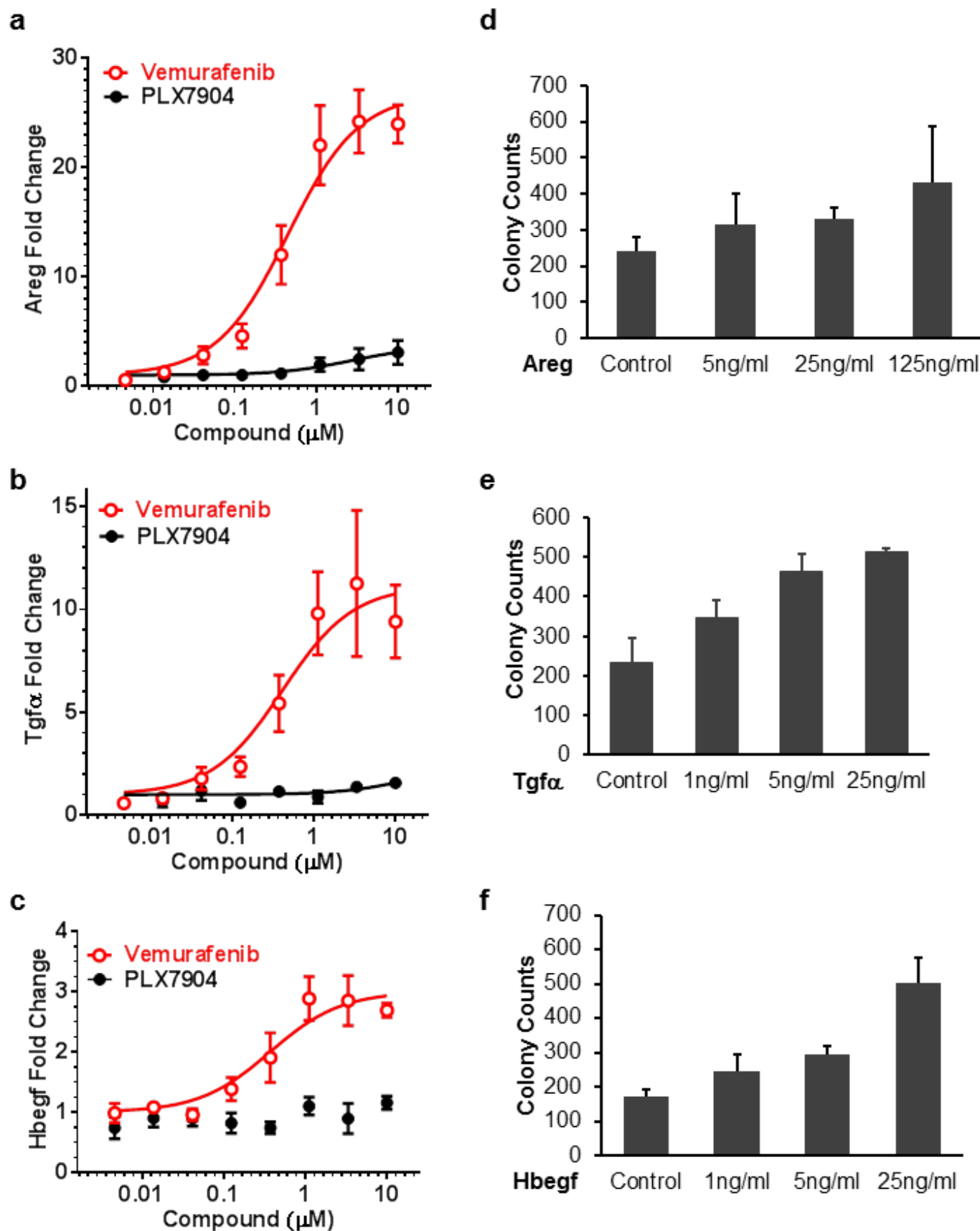
Extended Data Figure 1 | Differential effects of PLX7904 and vemurafenib on MAPK signalling. PLX7904 (black) and vemurafenib (red) show similar potency to block pERK signalling in human BRAF^{V600E} melanoma cell COLO829 (a); but in RAS activated human melanoma cell line IPC-298 (NRAS^{Q61L}) (b) and human colorectal carcinoma cell line HCT116 (KRAS^{G13D}) (c), vemurafenib paradoxically activates MAPK signalling while PLX7904 causes negligible pERK increase. d, Expanded view of the pERK

curves showing that PLX7904 inhibits pERK at high concentrations in three RAS mutant cell lines, with apparent IC_{50} ($\text{IC}_{50}^{\text{app}}$) values in the 100 μM range. Therefore, paradox breakers are not expected to affect the MAPK pathway in normal tissues (either paradoxical activation or inhibition) at therapeutic concentrations. The pERK curves were generated using an AlphaScreen assay. Mean \pm s.d., $n = 5$ independent experiments.



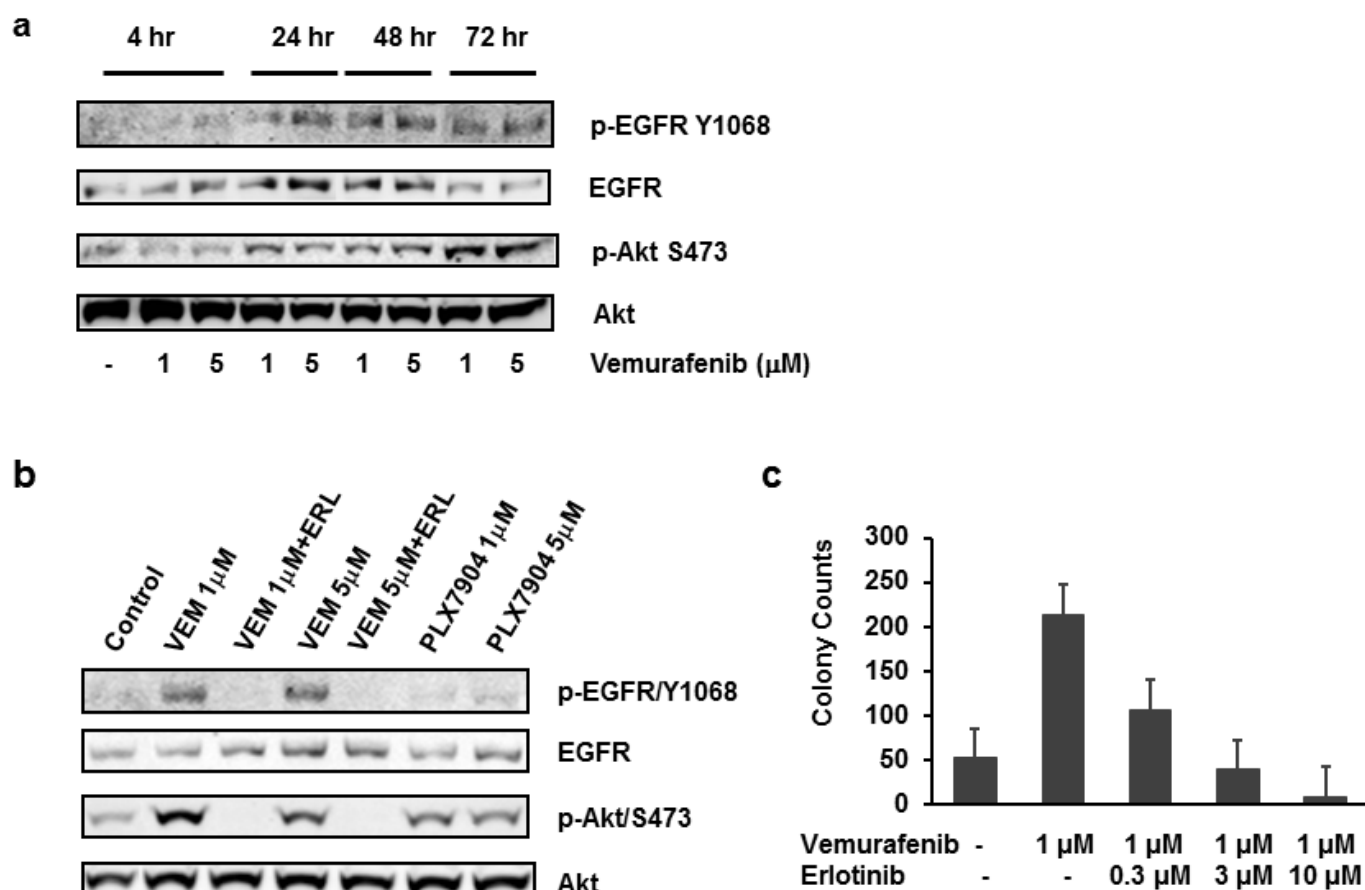
Extended Data Figure 2 | Gene expression analysis of B9 cells in response to either vemurafenib or PLX7904 treatment (both at 1 μ M concentration). **a, b**, Hierarchical clustering of the 236 Affymetrix mouse gene probes (see Supplementary Table 2 for a complete list) that were upregulated (**a**) or downregulated (**b**) by vemurafenib (233 probes) or PLX7904 (4 probes). The single overlap, *Cyp1b1*, and four representative MAPK pathway-responsive genes as well as three genes that encode EGFR ligands are marked. Two independent experiments are shown. MAPK pathway response genes *Spry2*,

Fos, and *Egr1* were upregulated by vemurafenib. The corresponding human genes are known to be suppressed by vemurafenib in BRAF^{V600E} mutant human melanoma³⁶. Opposing changes in expression were also observed with the *Id2* gene. **c**, Changes in the messenger RNA levels of four EGFR ligands (amphiregulin, HB-EGF, TGF- α , and epiregulin) along with EGFR itself in B9 cells treated with vemurafenib or PLX7904. All four EGFR ligands abundantly expressed in B9 cells were induced by vemurafenib, but the expression of EGFR and other ERBB family members remained unchanged.



Extended Data Figure 3 | EGFR ligands may mediate vemurafenib-induced cuSCC. ELISA assays demonstrate increased levels of amphiregulin (a) and TGF- α (b) proteins in the supernatants and HB-EGF (c) in the cell lysates of B9 cells after vemurafenib treatment for 48 h. PLX7904 does not induce the expression of EGFR ligands. Like vemurafenib, exogenous amphiregulin (d),

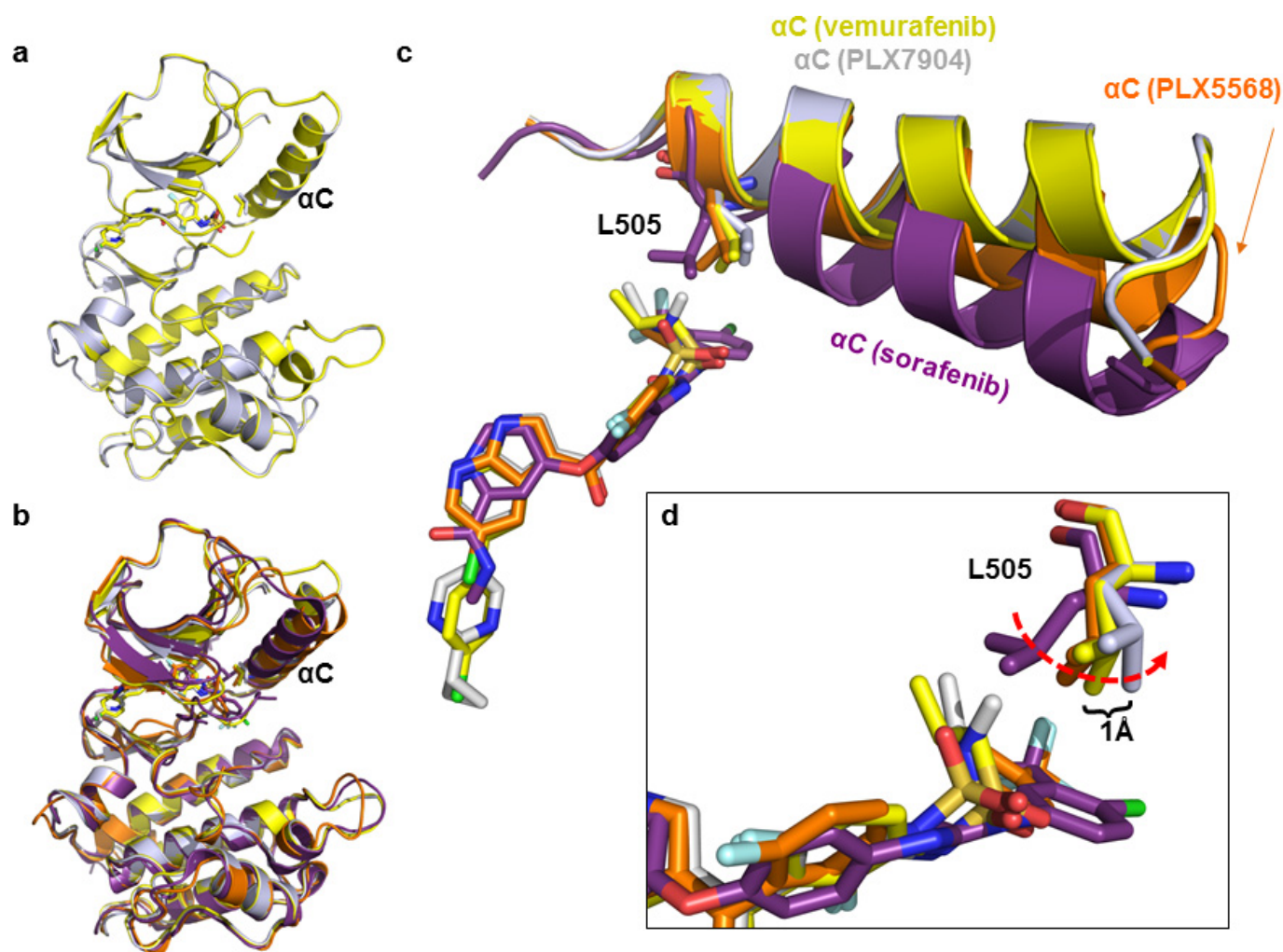
TGF- α (e), and HB-EGF (f) promote the anchorage-independent growth of B9 cells. B9 cells grown in soft agar were treated with EGFR ligands at the indicated concentrations for 3 weeks. Error bars, s.d. (a–c), s.e.m. (d–f); $n = 5$ (a–c) and 6 (d–f) independent experiments.



Extended Data Figure 4 | Effect of BRAF inhibitors on EGFR signalling.

a, EGFR signalling measured by levels of phosphorylated EGFR and AKT after a brief (10 min) exposure of serum-starved B9 cells to supernatant collected from B9 cells treated with vemurafenib for the indicated time. **b**, Pre-treatment with EGFR inhibitor erlotinib (ERL) inhibited EGFR signalling induced by supernatants from vemurafenib (VEM)-treated B9 cells. Serum-starved B9 cells were pre-treated with 3 μM erlotinib before starting a 10 min exposure to the

supernatants. Supernatants were collected from B9 cells treated with vemurafenib or PLX7904 for 3 days. **c**, Erlotinib inhibits the soft agar colony forming capacity of vemurafenib in B9 cells. Panels **a** and **b** are representative of results from three independent experiments. Error bars in **c**, s.e.m.; $n = 6$ independent experiments. Full scans of western blot data are presented in Supplementary Figure 1.

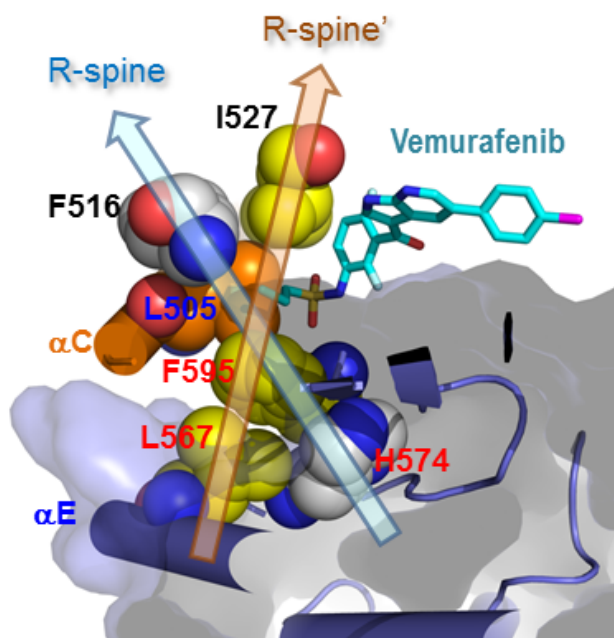


Extended Data Figure 5 | Comparison of inhibitor-bound BRAF structures.

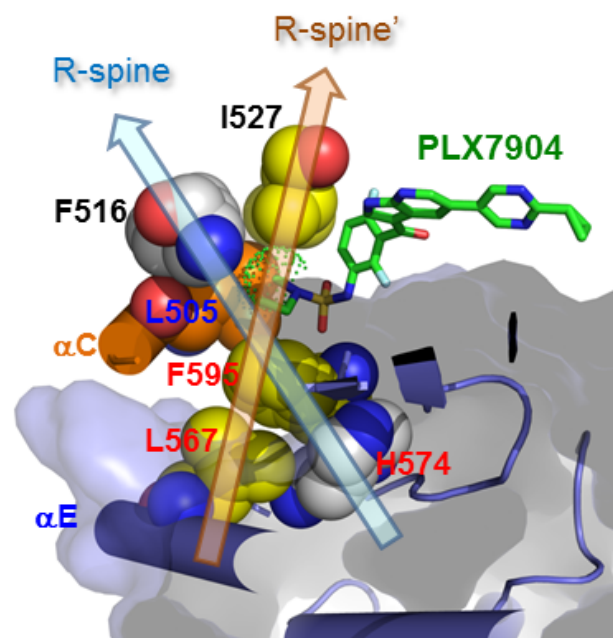
a, Perfect alignment between vemurafenib and PLX7904-bound BRAF structures (backbone root mean squared deviation 0.22 Å). **b**, An overlay of the structures of BRAF bound to four inhibitors: sorafenib, PLX5568, vemurafenib, and PLX7904 (colour schedule same as **c**). **c**, Outward movement of αC

helix in response to different inhibitors. From sorafenib to PLX5568 to vemurafenib, the degree of outward shift correlates with increasing ERK pathway inhibition index (Table 1). **d**, Close-up view showing the Leu505 side-chain position in the four structures. PLX7904 pushes the tip of Leu505 side-chain away by 1 Å from its position in the vemurafenib-bound structure.

a



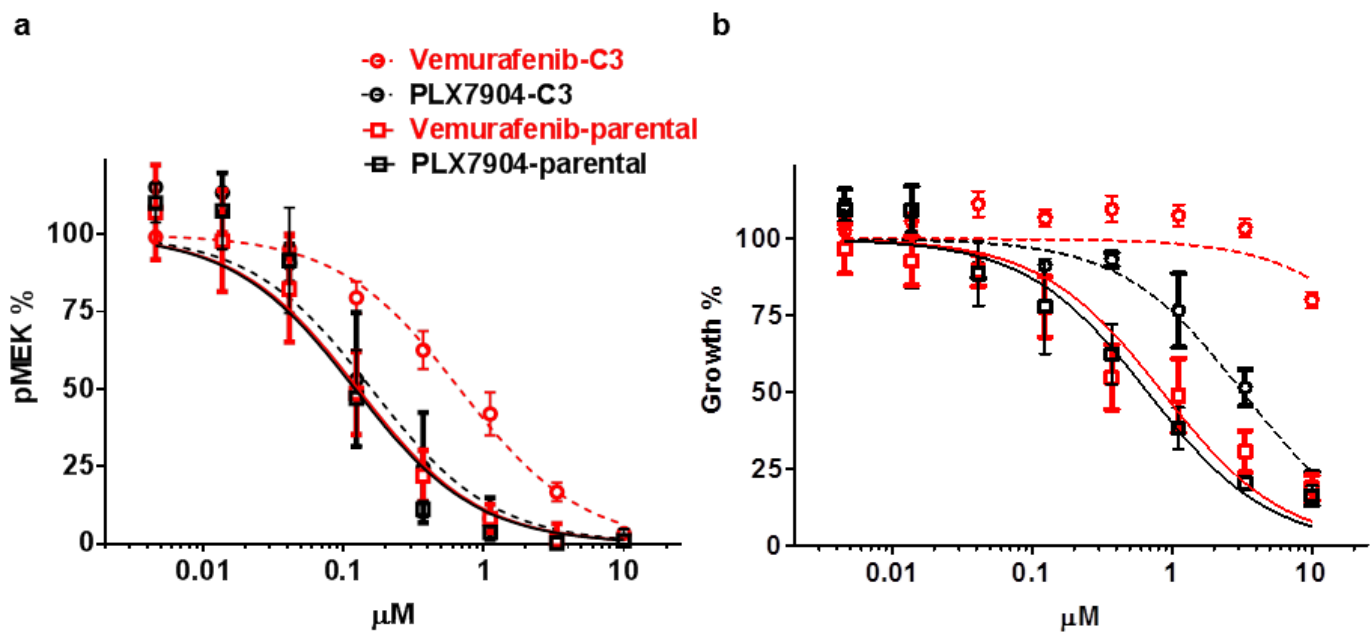
b



Extended Data Figure 6 | The regulatory spine (R-spine) in BRAF.

a, b, R-spine refers to four conserved hydrophobic residues that form a column in the active state of a kinase, and the distortion or disassembly of the spine marks the transition to an inactive state²². The term was introduced using PKA as the template, and the four residues that compose the R-spine included Leu95, Leu106, Tyr164, and Phe185 (PKA numbering). The corresponding residues in BRAF are Leu505, Phe516, His574, and Phe595 (rendered here in spheres). Tyr164 of PKA, which is a histidine (for example, His574 in BRAF) in most other kinases, forms hydrogen bonds with the backbone of the DFG motif and packs against the side chain of DFG Phe185 (the corresponding residue in

BRAF is Phe595). In the BRAF structure, Leu567 from α E helix also makes direct hydrophobic contacts with Phe595, an interaction that is conserved across the kinome. Leu567, Phe595, Leu505, along with another hydrophobic residue Ile527 that packs against Leu505, form a column (dubbed here as R-spine') with an axis tilted 45° from that of the R-spine. Analyses of published kinase structures show that all four R-spine' residues could be involved in kinase inhibitor binding whereas the two outer residues of R-spine rarely make direct contacts with inhibitors. Therefore, R-spine' is more relevant for studying inhibitor-induced conformational change in kinases.



Extended Data Figure 7 | Vemurafenib-resistant cells remain relatively sensitive to paradox breakers. a, pMEK and b, growth IC_{50} curves (mean \pm s.d., $n = 5$ experiments) for vemurafenib and PLX7904 in the

SKMEL-239 parental cell line and a representative vemurafenib-resistant clone (C3) that expresses a spliced variant of $\text{BRAF}^{\text{V600E}}$ promoting dimerization.

Extended Data Table 1 | Data collection and refinement statistics

| | BRAF ^{V600E} _ PLX7904 (PDB:4XV1)# | BRAF ^{V600E} _ Dabrafenib (PDB:4XV2)# | BRAF ^{V600E} _ PLX7922 (PDB:4XV3)# | BRAF ^{WT} _ PLX5568 (PDB:4XV9)# |
|---|---|---|---|--|
| Data collection | | | | |
| Space group | <i>P</i> 2 ₁ 2 ₁ 2 ₁ | <i>P</i> 2 ₁ 2 ₁ 2 ₁ | <i>P</i> 2 ₁ 2 ₁ 2 ₁ | <i>P</i> 4 ₃ 22 |
| Cell dimensions <i>a</i> , <i>b</i> , <i>c</i> (Å) | 51.3, 104.8, 110.2 | 53.7, 105.7, 109.7 | 51.9, 105.4, 111.3 | 119.3, 119.3, 52.5 |
| Resolution (Å) | 76.0-2.47 (2.58- 2.47) * | 109.7-2.50 (2.64- 2.50) | 111.3-2.80 (2.95- 2.80) | 50.0-2.00 (2.05- 2.00) |
| <i>R</i> _{sym} or <i>R</i> _{merge} | 0.077 (0.743) | 0.071 (0.531) | 0.108 (0.591) | 0.078 (0.354) |
| <i>I</i> / <i>σI</i> | 7.8 (1.0) | 8.1 (1.4) | 5.1 (1.5) | 6.9 (2.1) |
| Completeness (%) | 100.0 (100.0) | 99.9 (99.9) | 99.9 (100.0) | 99.9 (100.0) |
| Redundancy | 5.8 (5.9) | 6.1 (6.2) | 4.6 (4.8) | 13.6 (11.2) |
| Refinement | | | | |
| Resolution (Å) | 76.0-2.47 | 54.9-2.50 | 55.7-2.80 | 50.0-2.00 |
| No. reflections | 22,006 | 22,263 | 15,592 | 24,901 |
| <i>R</i> _{work} / <i>R</i> _{free} | 0.234/0.273 | 0.212/0.244 | 0.258/0.296 | 0.204/0.238 |
| No. atoms | | | | |
| Protein | 3912 | 3970 | 3864 | 2079 |
| Ligand/ion | 36 | 70 | 31 | 34 |
| Water | 40 | 54 | 44 | 256 |
| B-factors | | | | |
| Protein | 73 | 63 | 62 | 27 |
| Ligand/ion | 89 | 41 | 68 | 22 |
| Water | 56 | 48 | 35 | 35 |
| R.m.s deviations | | | | |
| Bond lengths (Å) | 0.003 | 0.003 | 0.003 | 0.006 |
| Bond angles (°) | 0.7 | 0.7 | 0.7 | 1.1 |

*Highest resolution shell is shown in parenthesis.

Data for each structure is collected from a single crystal.